A WCSPH Model for Numerical Investigation of Wave Impact on Vertical Structures

LEOPOLDO ANCORA, GIOVANNI CANNATA
Department of Civil, Constructional, and Environmental Engineering,
"Sapienza" University of Rome,
Via Eudossiana, 18 – 00184, Rome,
ITALY

Abstract: - This paper presents a numerical model based on the Weakly Compressible Smoothed Particle Hydrodynamics (WCSPH) method for simulating wave impact on vertical structures. The model incorporates kernel gradient correction, pressure field stabilization, and free-surface identification techniques, aimed at improving the accuracy and stability of the numerical solution. Validation is performed by comparing numerical results with experimental data from dam-break tests and regular wave impact tests against a vertical wall, showing agreement in terms of free-surface evolution and wall pressures. The model is then applied to investigate the impact of solitary waves on vertical structures in the presence of different seabed configurations. The results show that the model is capable of effectively reproducing both the quasi-hydrostatic distribution of pressures generated by non-breaking waves and the high-intensity, short-duration impulsive pressure peaks generated by breaking waves.

Key-Words: - WCSPH, wave impact, breaking waves, pressure evaluation, kernel gradient correction, free-surface flows.

Received: February 4, 2026. Revised: April 3, 2026. Accepted: June 16, 2026. Published: September 3, 2026.

1 Introduction

Vertical coastal protection structures, such as seawalls, quay walls, and vertical breakwaters, are designed to protect coastal areas and port infrastructure from wave action. The seaward face of these structures is subjected to horizontal forces generated by wave impact, whose accurate assessment is a crucial aspect of the structural design and safety assessment of coastal structures, [1].

In the case of non-breaking waves, the primary effect of the impact can be attributed to a resultant horizontal force which, as a first approximation, can be described by a quasi-hydrostatic pressure distribution. Under these conditions, the applied load depends primarily on the maximum run-up of the free surface reached during the impact and can be estimated using well-established analytical formulations, [2]. Conversely, when a breaking wave approaches a vertical wall, the transformation of the wave profile and the steepening of the wavefront are accompanied by a significant increase in the horizontal component of the fluid particle velocity, generating violent impacts and high-intensity, short-duration loads, [3], [4]. The magnitude of the forces and their distribution along the wall depend critically on the geometry of the wavefront immediately prior to impact, making the prediction of this phenomenon particularly complex, [5], [6].

Generally, the estimation of loads induced by breaking-wave impacts is performed using empirical formulations, [1], [7], [8] derived from laboratory experimental campaigns, [9], [10]. The significant scatter in experimental results makes the estimation of wave-induced loads particularly challenging. Furthermore, laboratory tests present inherent limitations related to scale effects, which may affect the representativeness of the results under full-scale conditions. Therefore, numerical simulations capable of describing the highly nonlinear dynamics of wave breaking and wave-structure interaction represent a valuable tool for extending the analysis to prototype-scale conditions, [11], [12], [13], [14].

Numerical simulation of wave breaking and wave–structure interaction has been the subject of extensive research. The most traditional numerical approach to studying such problems involves the use of mesh-based schemes, in which the main challenge lies in simulating changes in the position and shape of the free surface. The main strategies for solving this problem are based on techniques such as the Volume of Fluid (VOF) method [15], [16], the Level Set method [17], [18], and dynamic transformations of the vertical coordinate (σ-coordinates) onto a regular [19] or curvilinear [20], [21] coordinate system.

As highlighted by several numerical studies[22], [23], the simulation of irregular and fragmented breaking wave fronts and the associated impulsive pressure peaks using the aforementioned techniques can be particularly computationally demanding, if not prohibitive. This represents a significant limitation in the simulation of wave impact on vertical walls, where small variations in the kinematics of the wave front can lead to significant differences in the estimated loads, [24].

Lagrangian meshless methods, based on a particle discretization of the fluid, represent a particularly effective alternative to mesh-based methods, as they naturally describe fluid motion even in the presence of large free-surface deformations. Among these, Weakly Compressible Smoothed Particle Hydrodynamics (WCSPH), originally introduced in astrophysics [25], [26] and subsequently extended to free-surface flows [27], is now widely used in the simulation of coastal hydrodynamics and fluid–structure impact problems. The Lagrangian formulation of the method allows for a natural description of fluid motion even in the presence of highly deformed free surfaces, spray, and fluid fragmentation. However, the application of the WCSPH method still presents several challenges related mainly to the consistency of the discrete approximation, free-surface particle identification, and pressure-field stability, [28], [29], [30].

This paper presents a numerical model based on the WCSPH method, incorporating strategies aimed at improving the consistency of the discrete approximation and mitigating the main sources of error affecting the accuracy and stability of the solution. In particular, a kernel gradient correction technique [31] and a particle repositioning procedure [32] are adopted to improve the consistency of the discretization; a diffusive term is also introduced into the continuity equation to stabilize the pressure field [33]; finally, a free-surface identification procedure based on a multi-criterion approach combining physical and geometric parameters is implemented, [30]. The resulting model is intended for the simulation of wave impact on vertical-wall structures and, more specifically, for the evaluation of the impulsive pressure peaks, with particular attention to their spatial and temporal distribution.

The proposed model is validated against benchmark cases involving the propagation of regular and breaking waves and fluid impacts against rigid walls. The model is then applied to the simulation of wave impact on a vertical-wall coastal defense structure, considering both horizontal beds, where waves do not break, and sloping beds, where wave breaking occurs. The pressure time histories induced by wave impact against the wall, together with the maximum values recorded during the event, provide essential insights into the mechanisms governing the generation and spatial localization of horizontal loads on vertical walls.

The remainder of the paper is organized as follows. Section 2 introduces the numerical method, presenting the WCSPH model and the specific numerical strategies adopted for the accurate simulation of the investigated phenomena. Section 3 presents the validation of the model against experimental data available in the literature concerning dam-break flows impacting a vertical wall and regular breaking wave trains impacting a vertical wall. Section 4 is devoted to the investigation of the propagation and impact of two solitary waves ($H_{w1} = 1.25\,m$, $H_{w2} = 1.50\,m$) against a vertical wall, considering two different seabed configurations: a horizontal bed and a sloping bed with a $1:20$ slope.

2 Numerical Model

The numerical model is based on the Weakly Compressible Smoothed Particle Hydrodynamics (WCSPH) method, in which the fluid domain is represented by a set of particles that move following the fluid motion and carry the fluid's physical properties, such as mass, density, and velocity, [27]. A key advantage of the adopted method is the possibility of calculating the value of a physical quantity and its gradient through a convolution integral over a finite support domain. Within this approach, physical quantities are approximated using a kernel function W, which defines the influence of neighbouring particles within a region whose extent is controlled by the smoothing length h. In continuous form, a generic scalar field $A(\boldsymbol{r})$ is expressed as

$$A(\boldsymbol{r}) = \int_{\Omega} A(\boldsymbol{r}')W(\boldsymbol{r}-\boldsymbol{r}',h)\,d\boldsymbol{r}' \qquad (1)$$

where Ω represents the support domain of the kernel function W.

The accuracy of the SPH approximation depends on the properties of the adopted kernel function, [22], [23], [26]. In particular, the kernel must satisfy the normalization condition

$$\int_{\Omega} W(\boldsymbol{r}-\boldsymbol{r}',h)\,d\boldsymbol{r}' = 1 \tag{2}$$

which guarantees the exact reproduction of constant fields. Indeed, for a constant function $f(\boldsymbol{r}) = c$,

$$\int_{\Omega} c\,W(\boldsymbol{r}-\boldsymbol{r}',h)\,d\boldsymbol{r}' = c \tag{3}$$

thereby confirming the zeroth-order consistency of the SPH approximation.

Moreover, the kernel must satisfy the symmetry condition

$$\int_{\Omega} (\boldsymbol{r}'-\boldsymbol{r})W(\boldsymbol{r}-\boldsymbol{r}',h)\,d\boldsymbol{r}' = 0 \tag{4}$$

which guarantees the exact reproduction of linear field variations. Accordingly, for a linear function $f(\boldsymbol{r}) = c_0 + \boldsymbol{c_1}\cdot\boldsymbol{r}$, the kernel approximation satisfies

$$\int_{\Omega} (c_0 + c_1\cdot\boldsymbol{r}')\,W(\boldsymbol{r}-\boldsymbol{r}',h)\,d\boldsymbol{r}' = c_0 + \boldsymbol{c_1}\cdot\boldsymbol{r} \tag{5}$$

thereby establishing the first-order consistency of the SPH approximation.

The normalization and symmetry conditions (Eqs. 2, 4) ensure the exact reproduction of constant and linear fields, respectively. More generally, to exactly reproduce polynomial fields up to the $n-th$ order, the kernel must satisfy

$$\begin{aligned} M_0 &= \int_{\Omega} W(\boldsymbol{r}-\boldsymbol{r}',h)\,d\boldsymbol{r}' = 1, \\ M_k &= \int_{\Omega} (\boldsymbol{r}'-\boldsymbol{r})^k W(\boldsymbol{r}-\boldsymbol{r}',h)\,d\boldsymbol{r}' = 0, \\ k &= 1,\dots,n \end{aligned} \tag{6}$$

where M_k denotes the $k-th$ kernel moment. These conditions provide the theoretical basis for achieving the $n-th$ order consistency of the SPH interpolation, [22], [23].

By analogy, a set of consistency conditions can be derived for the SPH gradient operator, [22], [23]. In order to reproduce polynomial derivatives up to the $n-th$ order, the kernel gradient should satisfy the corresponding moment conditions,

$$M_0^{\nabla} = \int_{\Omega} \nabla W(\boldsymbol{r}-\boldsymbol{r}',h)\,d\boldsymbol{r}' = 0, \tag{7}$$

$$\begin{aligned} M_1^{\nabla} &= \int_{\Omega} (\boldsymbol{r}'-\boldsymbol{r})\otimes\nabla W\big(\boldsymbol{r}-\boldsymbol{r}',h\big)\,d\boldsymbol{r}' = \boldsymbol{I} \\ M_k^{\nabla} &= \int_{\Omega} (\boldsymbol{r}'-\boldsymbol{r})^k\otimes\nabla W(\boldsymbol{r}-\boldsymbol{r}',h)\,d\boldsymbol{r}' = 0,\quad k=2,\dots,n \end{aligned}$$

where $\boldsymbol{I}$ denotes the identity tensor.

In the present work, a Wendland kernel function [34], is adopted due to its high stability and reduced sensitivity to particle clustering.

In discrete form, the integral representation of Eq. 1 is replaced by a summation over the contributions of neighboring particles

$$A(\boldsymbol{r}_i) = \sum_{j\in\Omega} A(\boldsymbol{r}_j)\frac{m_j}{\rho_j}W_{ij}(\boldsymbol{r}_{ij},h) \tag{8}$$

where m_j and ρ_j represent the mass and density of a particle j, [26].

The spatial derivatives of the function $A(\boldsymbol{r})$ are calculated by applying the differential operator directly to the kernel function W, owing to the compact support of W

$$\nabla A(\boldsymbol{r}_i) = \sum_{j\in\Omega} A(\boldsymbol{r}_j)\frac{m_j}{\rho_j}\nabla W_{ij}(\boldsymbol{r}_{ij},h) \tag{9}$$

In line with the SPH discretization, the continuity and momentum conservation equations can be written as [35]

$$\begin{aligned} \frac{d\rho_i}{dt} &= \rho_i\sum_{j\in\Omega}\frac{m_j}{\rho_j}(\boldsymbol{v_i}-\boldsymbol{v_j})\cdot\nabla_i W_{ij} \\ \frac{d\boldsymbol{v}_i}{dt} &= -\sum_{j\in\Omega} m_j\left(\frac{p_j}{\rho_j^2}+\frac{p_i}{\rho_i^2}+\boldsymbol{\Pi_{ij}}\right)\nabla_i W_{ij} - \boldsymbol{g} \end{aligned} \tag{10}$$

where $\boldsymbol{\Pi_{ij}}$ denotes the artificial viscosity term adopted to stabilize the numerical solution [26]. The pressure field is evaluated through the following equation of state

$$p = c_0^2(\rho-\rho_0) \tag{11}$$

which introduces an artificial fluid compressibility through the parameter c_0, whose value is selected to keep relative density fluctuations below approximately 1% of the reference density ρ_0.

2.1 Density Diffusion Term

In the presence of anisotropic particle distributions and incomplete kernel support domains, the SPH approximation introduces errors in the evaluation of physical quantities and of the associated differential operators, thereby compromising the local consistency of the scheme. In particular, errors in the discretization of the divergence of the velocity field appearing in the continuity equation may generate irregular density fields and spurious pressure oscillations. In the proposed model, in order to suppress these spurious oscillations, a diffusive term acting exclusively on the dynamic component of the pressure is introduced into the continuity equation, [36].

$$\frac{d\rho_i}{dt} = \rho_i \sum_{j\in\Omega} \frac{m_j}{\rho_j}\left(\boldsymbol{v_i} - \boldsymbol{v_j}\right)\cdot \nabla_i W_{ij} + \delta\ h\, c_0 \sum_{j\in\Omega} V_j\ \boldsymbol{\psi}_{ij}\, \nabla_i W_{ij} \tag{12}$$

where the term $\boldsymbol{\psi}_{ij}$ is expressed as follows [33]

$$\boldsymbol{\psi}_{ij} = 2\left(\Delta\rho_j^D - \Delta\rho_i^D\right)\frac{\boldsymbol{r}_{ij}}{\left|\boldsymbol{r}_{ij}\right|^2} \tag{13}$$

where

$$\Delta\rho_i^D = \Delta\rho_i - \Delta\rho_i^H \tag{14}$$

and

$$\Delta\rho_i = \rho_i - \rho_0. \tag{15}$$

The hydrostatic component $\Delta\rho_i^H$ is evaluated consistently with Eq. 11.

$$\Delta\rho_i^H(y) = \frac{\rho_0\ g\ (\eta - y_i)}{c_0^2}. \tag{16}$$

where y_i is the elevation of a particle i relative to the bottom and η is the free-surface elevation.

2.2 Kernel Gradient Correction

Although the kernel-gradient moment conditions introduced in Section 2 are satisfied in the continuous formulation, they are generally no longer exactly fulfilled after particle discretization because of particle disorder, incomplete kernel support, and quadrature errors. As a consequence, the discrete SPH gradient operator loses first-order consistency, leading to inaccurate evaluations of spatial derivatives, particularly in the vicinity of free surfaces and boundaries. To restore first-order consistency, a local correction matrix $\boldsymbol{L}_i$ is applied to the gradient of the kernel function W, [31].

In the present formulation, the corrected kernel gradient is employed in the discretization of the pressure-gradient term of the momentum equation in Eq. 10. Since the prediction of impulsive wave loads relies on an accurate evaluation of pressure gradients, restoring the first-order consistency of the discrete gradient operator is expected to improve the numerical accuracy of the pressure gradient evaluation, particularly during violent wave impacts.

$$\nabla_i W_{ij} \rightarrow \boldsymbol{L}_i \nabla_i W_{ij} \tag{17}$$

The correction matrix $\boldsymbol{L}_i$ is computed so as to restore the discrete counterpart of the M_1^{∇} condition in Eq. 7.

$$\left(\sum_{j\in\Omega} \frac{m_j}{\rho_j}\boldsymbol{r}_{ij} \otimes \nabla_i W_{ij}\right)\boldsymbol{L}_i^T = \boldsymbol{I}\,. \tag{18}$$

which guarantees the exact evaluation of the gradients of linearly varying scalar fields [31].

The matrix $\boldsymbol{L}_i$ is therefore computed as:

$$\boldsymbol{L}_i = \left(\sum_{j\in\Omega} \frac{m_j}{\rho_j}\nabla_i W_{ij} \otimes \boldsymbol{r}_{ij}\right)^{-1} \tag{19}$$

and is referred to as the kernel-gradient renormalization matrix.

2.3 Free-surface Identification

The introduction of corrective techniques into the standard SPH formulation, such as the application of the renormalization matrix $\boldsymbol{L}_i$ to the gradient of the kernel function W [31], requires an explicit treatment of the free surface. Under these conditions, the zero-pressure condition at the fluid–air interface is no longer implicitly satisfied and requires the identification of free-surface particles. An inaccurate identification of the free surface may introduce errors in the evaluation of the pressure field and compromise numerical stability, especially in the presence of highly deformed or fragmented free surfaces, [30]. The adoption of criteria based solely on local parameters [37], [38], such as the ratio between the computed and reference density or the filling degree of the kernel support domain, may prove insufficiently robust during phases characterized by strong free-surface deformation. In the presence of highly dynamic interfaces, multi-criterion approaches combining physical and geometric information allow for a more consistent classification of free-surface particles. In the present work, the procedure proposed in [30], is adopted, based on the combined analysis of the density ratio of the particle i

$$\alpha_i = \frac{\rho_i}{\rho_0} \tag{20}$$

and of the particle distribution in the neighborhood of the particle i, described through auxiliary geometric functions, [30]. Particle i is therefore identified as belonging to the free surface when at least one of the criteria proposed in [30], combining the analysis of the density ratio and the auxiliary geometric functions is satisfied.

3 Validation

Validation is performed by comparing the numerical results produced by the proposed model with experimental data obtained from laboratory tests, [39], [40]. The reproduced experiments concern a two-dimensional dam-break test [39] and a regular breaking-wave train propagating and impacting against a vertical wall, [40].

3.1 Dam-break

The dam-break test is a classical benchmark for the validation of numerical models aimed at investigating violent fluid–structure impacts. The experimental configuration proposed in [39] shown in Figure 1 consists of the collapse of a water column with a height $H = 300\,mm$ over a dry horizontal bottom of length $L = 1610\,mm$, at the end of which a vertical wall instrumented with four pressure sensors is positioned. The sensors are located at elevations $z_{P_1} = 3\,mm$, $z_{P_2} = 15\,mm$, $z_{P_3} = 30\,mm$, $z_{P_4} = 80\,mm$, respectively. A particle diameter (dx) of 5 mm was adopted.

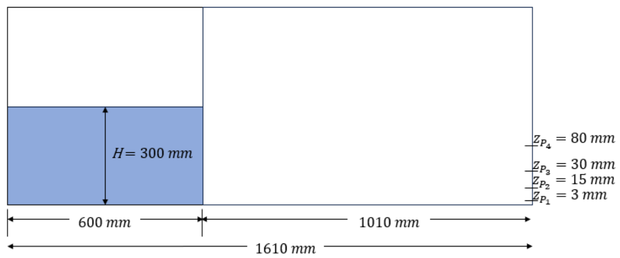

Fig. 1: schematic layout of the experimental setup proposed in [39].
Source: created by the authors.

Once the collapse of the water column is initiated, the wave front propagates toward the wall, reaching it at $t = 0.439\,s$. Figure 2 shows a comparison between the numerical results obtained with the WCSPH model and the experimental data from [39], in terms of the time evolution of the wave-front position along the horizontal bottom.

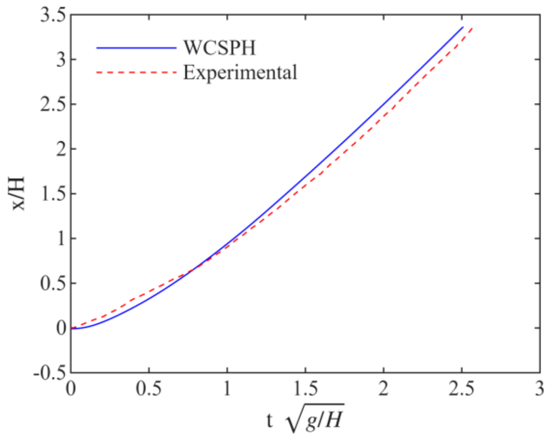

Fig. 2: time evolution of the numerical and experimental wave-front propagation over the horizontal bottom [39].
Source: created by the authors.

To further assess the accuracy of the numerical results related to wave-front propagation over the bottom, a comparison with the experimental data from [39] was also performed (Figure 3) in terms of the free-surface elevation h over time at the location $x = 300\,mm$.

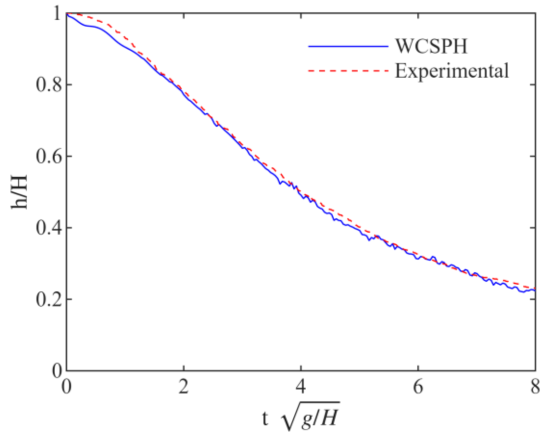

Fig. 3: time evolution of the free-surface elevation at $x = 300\,mm$, comparison between numerical results and experimental data from [39].
Source: created by the authors.

The numerical analysis was further extended to the time histories of the pressures recorded by the four sensors mounted on the wall (Figure 4, Figure 5, Figure 6 and Figure 7). Consistent with the experimental observations reported in [39], the numerical results show a progressive decrease in the maximum pressure value measured by each sensor as the elevation of the sensor increases. Table 1 reports the relative error, $E\,(\%)$, computed as:

$$E(\%) = \frac{\left|X_{num} - X_{exp}\right|}{X_{exp}} \times 100 \qquad (21)$$

between the experimental [39] and numerical peak pressures associated with each sensor.

Table 1. E (%) in the numerical peak pressure estimates relative to the experimental data from [39] at each sensor location.

$sensor$	E (%)
z_{P_1}	3.21
z_{P_2}	11.83
z_{P_3}	6.58
z_{P_4}	10.64

Source: created by the authors

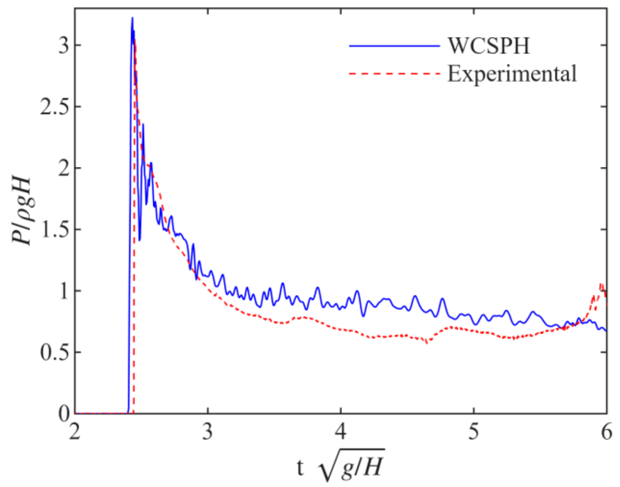

Fig. 4: pressure-time history at z_{P_1}: comparison between numerical results and experimental data from [39].
Source: created by the authors.

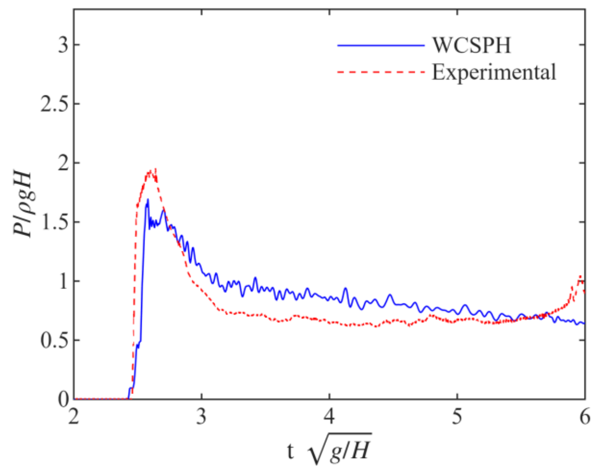

Fig. 5: pressure time history at z_{P_2}: comparison between numerical results and experimental data from [39].
Source: created by the authors.

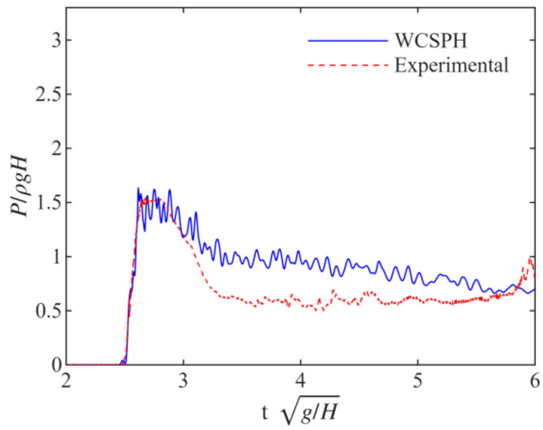

Fig. 6: pressure-time history at z_{P_3}: comparison between numerical results and experimental data from [39].
Source: created by the authors.

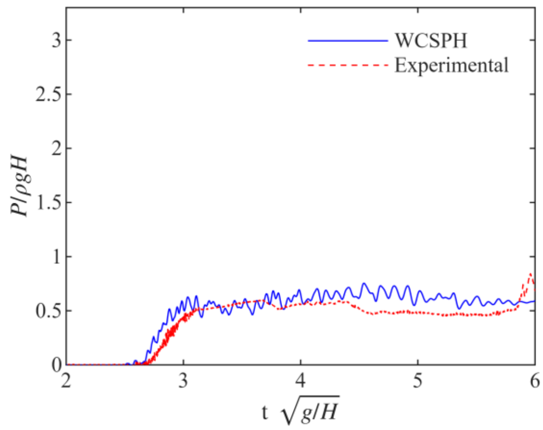

Fig. 7: pressure-time history at z_{P_4}: comparison between numerical results and experimental data from [39].
Source: created by the authors.

The shape of the pressure signals shown in Figure 4, Figure 5, Figure 6 and Figure 7 indicates that the impact is more violent at lower elevations, where higher pressure peaks occur and decay rapidly. In order to further verify the capability of the model to reproduce violent impacts, in addition to the maximum pressure value, the pressure impulse induced by the impact of the wave front was also evaluated at z_{P_1}. The impulse estimated by the proposed model, $I = 4.87\ mbar \cdot s$, was found to be slightly underestimated with respect to the experimental value of $5.15\ mbar \cdot s$, while still remaining well within the confidence intervals reported in [39].

3.2 Regular Waves Impacting a Vertical Wall

The second validation case selected for the numerical model concerns the interaction between a regular wave train and a vertical wall. The configuration of the reference experimental setup from [40] is shown in Figure 8. The still-water depth is $H = 266\,mm$. The incident waves are characterized by a period $T_w = 1.3\,s$ and a wave height $H_w = 100\,mm$. A particle diameter (dx) of $10\,mm$ was adopted.

In the numerical simulation, wave generation is performed using a piston wavemaker driven according to the same motion law adopted in the experimental case, [40].

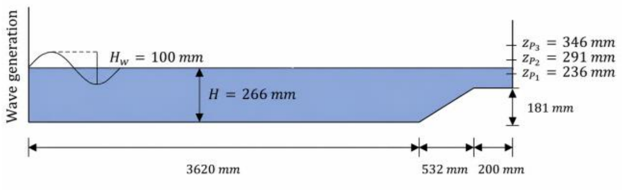

Fig. 8: schematic layout of the experimental setup proposed in [40].
Source: created by the authors.

The first comparison between the experimental results from [40] and the numerical results were carried out in terms of the time evolution of the free-surface elevation η at a vertical section located $2643\,mm$ from the wavemaker under still-water conditions (Figure 9).

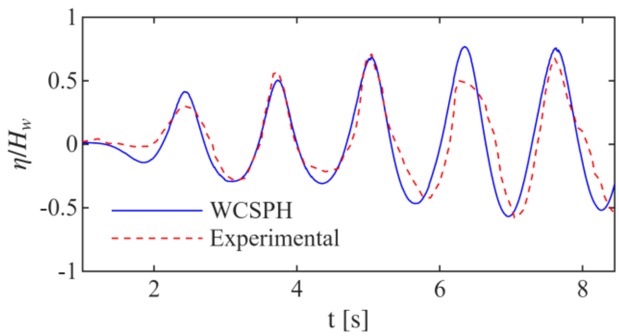

Fig. 9: time evolution of the free-surface elevation at $2643\,mm$ from the wavemaker at rest: comparison between numerical and experimental results from [40].
Source: created by the authors.

The pressure time histories are shown in Figure 10, Figure 11 and Figure 12 and correspond to the measurement points located at $z_{P_1} = 236\,mm$, $z_{P_2} = 291\,mm$ and $z_{P_3} = 346\,mm$. The numerical results obtained with the WCSPH model are presented together with the experimental data from [40], allowing for both qualitative and quantitative comparisons in terms of pressure evolution over time and peak pressure values, p_{max}.

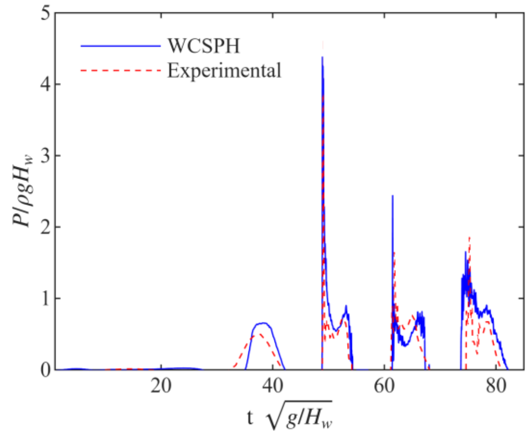

Fig. 10: pressure-time history at z_{P_1}: comparison between numerical and experimental results from [40].
Source: created by the authors.

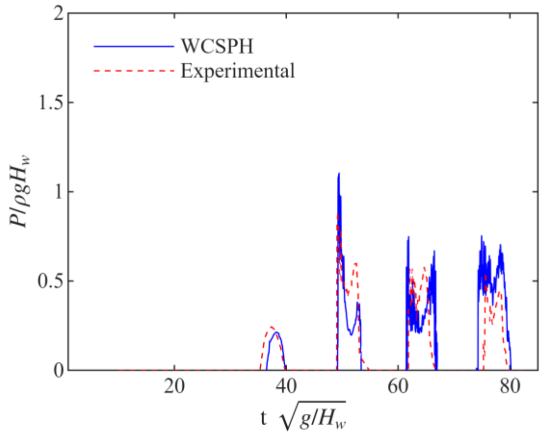

Fig. 11: pressure-time history at z_{P_2}: comparison between numerical and experimental results from [40].
Source: created by the authors.

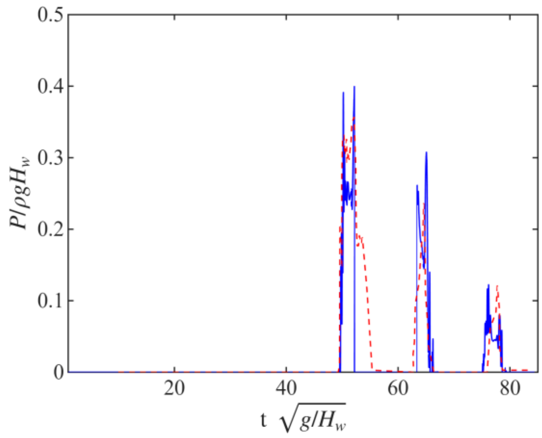

Fig. 12: pressure-time history at z_{P_3}: comparison between numerical and experimental results from [40].
Source: created by the authors.

Table 2 reports the E (%) between the numerical and experimental [40] peak pressure values recorded by each sensor during the test.

Table 2. E (%) in the numerical peak pressure estimates relative to the experimental data from [40] at each sensor location.

$sensor$	E (%)
z_{P_1}	13.17
z_{P_2}	23.73
z_{P_3}	12.07

Source: created by the authors.

3.3 Discussion on the Numerical Performance of the Proposed Formulation

The proposed formulation was evaluated under two different flow regimes, namely dam-break impact and regular wave loading against a vertical wall. In both cases, the numerical results are in good agreement with the experimental measurements in terms of free-surface evolution and pressure time histories, demonstrating the capability of the model to reproduce both the hydrodynamic evolution of the flow and the associated impact loads. Beyond the overall agreement with the experimental observations, these results provide a basis for interpreting the numerical behavior of the proposed formulation in light of the methodology introduced in Section 2.

Accurate prediction of wave impact loads relies on the correct evaluation of the pressure-gradient term appearing in the momentum equation. The evaluation of this term depends on two complementary aspects: the regularity of the pressure field and the consistency of the discrete gradient operator. The former is addressed by the density diffusion term, which reduces spurious density fluctuations. Through the adopted equation of state, this results in a smoother dynamic pressure field. The latter is addressed by the Kernel Gradient Correction, which restores the first-order consistency of the discrete gradient operator employed in the momentum equation. Since hydrodynamic forces are evaluated from the pressure-gradient term, improving both the regularity of the pressure field and the consistency of the gradient operator contributes to a more reliable prediction of the resulting impact loads. While the individual contribution of each numerical treatment cannot be isolated from the present validation study, the overall agreement with the experimental measurements is consistent with the complementary action of these two mechanisms. This suggests that simultaneously improving the regularity of the pressure field and the consistency of the gradient operator is beneficial for the prediction of impulsive pressure loads.

It is well established that, in particle-based Lagrangian methods, the spatial resolution of numerical simulations is primarily governed by the particle diameter (dx). It is also well known that reducing the particle diameter leads to a substantial increase in computational cost, which is generally not accompanied by a proportional improvement in simulation accuracy. To achieve an appropriate balance between accuracy enhancement and computational efficiency, several numerical simulations were performed for each of the two calibration test cases by progressively halving the particle diameter. For both test cases, the spatial resolution was considered adequate when the percentage reduction in the error resulting from further particle refinement was less than 50%.

Table 3 and Table 4 show a systematic reduction of both the absolute and relative errors as the particle spacing decreases. Although no formal order of convergence is estimated, the monotonic reduction of the error observed in both validation cases indicates a convergent behavior of the proposed formulation towards the experimental measurements. The same trend is observed for both the pressure impulse in the dam-break test and the peak pressure in the wave-impact experiment, despite the latter representing a considerably more demanding quantity because of its highly localized and impulsive nature. Considering the limited improvement achieved with the finest particle resolution relative to the associated increase in computational cost, the adopted discretization represents an effective compromise between numerical accuracy and computational efficiency.

Table 3. Comparison between the numerical and experimental pressure impulse related to z_{P_1} sensor for different particle spacings (dx). Absolute and relative errors are reported with respect to the experimental value.

dx $[mm]$	$I\ [mbar \cdot s]$	$E\ [mbar \cdot s]$	E (%)
20	4.18	0.97	18.83
10	4.69	0.46	8.93
5	4.87	0.28	5.44
$Exp.$	5.15		

Source: created by the authors.

Table 4. Comparison between the numerical and experimental peak pressure values recorded by z_{P_1} sensor for different particle spacings (dx). Absolute and relative errors are reported with respect to the experimental value.

dx $[mm]$	$P_{max}/\rho g H_w$	E	E (%)
40	5.48	1.73	46.13
20	4.57	0.82	21.84
10	4.26	0.55	13.17
$Exp.$	3.75		

Source: created by the authors.

4 Case Studies

The validated WCSPH model is applied to investigate the interaction between a solitary wave and a vertical wall. Two seabed configurations (Figure 13) and two distinct waves, characterized by $H_{w1} = 1.25\, m$ and $H_{w2} = 1.50\, m$, are considered. The first configuration consists of a horizontal bed $75\, m$ long with constant depth $H = 3.00\, m$. The second configuration is characterized by a $25\, m$ long horizontal seabed followed by $50\, m$ long sloping ramp with a slope of $1{:}20$. The two configurations are referred to as Configurations 1 and 2, respectively. In Configuration 1, the horizontal bed allows the wave to preserve its shape up to the impact, whereas in Configuration 2, the presence of the sloping ramp promotes wave breaking before the interaction with the wall. A total of four test cases are presented by varying both the wave height and the bottom slope over which the wave propagates. The results are presented in two subsections, each corresponding to a different wave height.

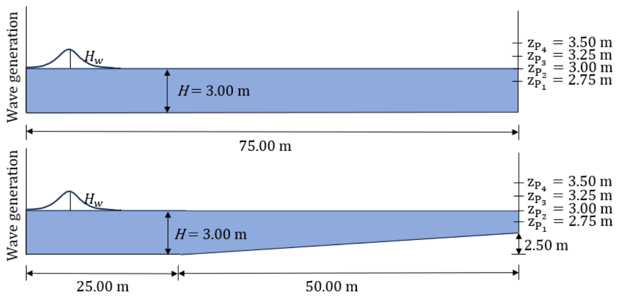

Fig. 13: schematic layout of Configurations 1 and 2.
Source: created by the authors.

4.1 Wave Impact Generated by the $H_{w1} = 1.25\, m$ Solitary Wave

Figure 14, Figure 15, Figure 16 and Figure 17 show the pressure time histories computed at the locations of the four sensors (z_{P1}, z_{P2}, z_{P3}, z_{P4}) during wave impact for Configurations 1 and 2.

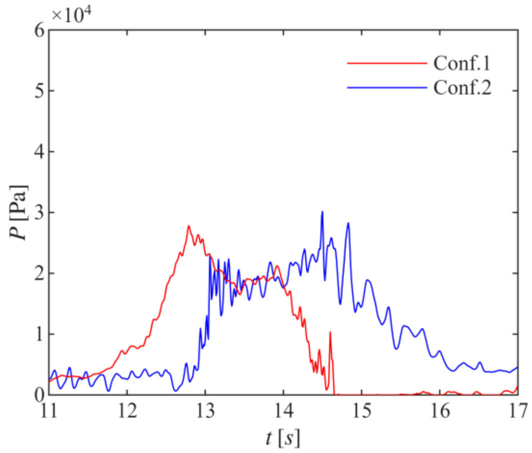

Fig. 14: pressure time histories at z_{P1} for Configurations 1 and 2.
Source: created by the authors.

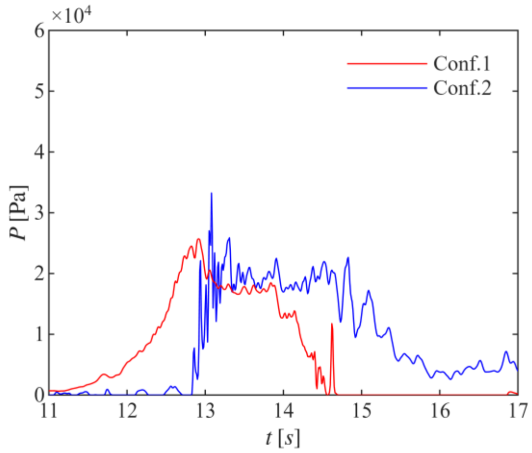

Fig. 15: pressure time histories at z_{P2} for Configurations 1 and 2.
Source: created by the authors.

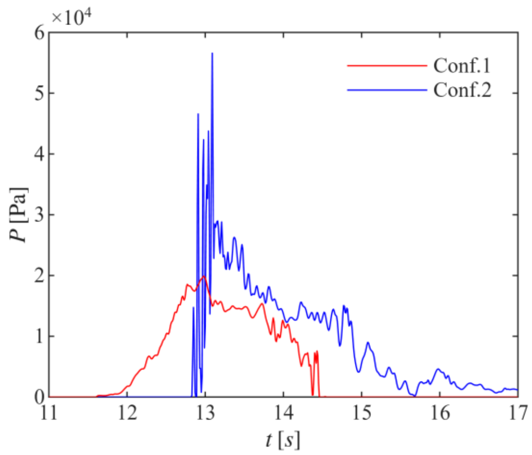

Fig. 16: pressure time histories at z_{P3} for Configurations 1 and 2.
Source: created by the authors.

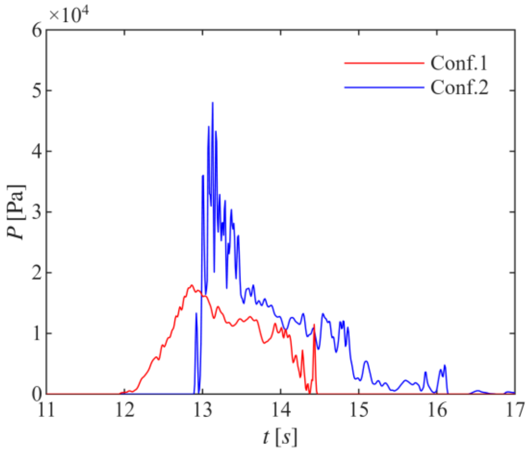

Fig. 17: pressure time histories at z_{P4} for Configurations 1 and 2.
Source: created by the authors.

The peak pressure values computed at the sensor locations for each configuration are reported in Table 5. Table 6 and Table 7 summarize the values of the pressure impulse, I, and the significant rise time associated with the pressure increase, rt. Both quantities, rt and I, are evaluated according to the definition provided in [11].

Table 5. Peak pressure values obtained from the numerical simulations for Configurations 1 and 2 with $H_{w1} = 1.25\ m$.

$sensor$	P_{max} $[Pa]$	
	Conf.1	Conf.2
z_{P_1}	27824	30173
z_{P_2}	25690	33250
z_{P_3}	19896	56590
z_{P_4}	17956	48033

Source: created by the authors.

Table 6. Pressure impulse values obtained from the numerical simulations for Configurations 1 and 2 with $H_{w1} = 1.25\ m$.

$sensor$	I $[Pa \cdot s]$	
	Conf.1	Conf.2
z_{P_1}	42011	46667
z_{P_2}	36757	46582
z_{P_3}	28339	8755
z_{P_4}	23113	19124

Source: created by the authors.

Table 7. Significant pressure rise-time values obtained from the numerical simulations for Configurations 1 and 2 with $H_{w1} = 1.25\ m$.

$sensor$	rt $[s]$	
	Conf.1	Conf.2
z_{P_1}	0.37	1.16
z_{P_2}	0.44	0.04
z_{P_3}	0.53	0.09
z_{P_4}	0.32	0.07

Source: created by the authors.

4.2 Wave Impact Generated by the $H_{w2} = 1.50\ m$ Solitary Wave

The pressure time histories induced by wave impact against the wall are shown in Figure 18, Figure 19, Figure 20 and Figure 21. The quantities characterizing the impact, similar to the case $H_{w1} = 1.25\ m$, are summarized in Table 8, Table 9 and Table 10.

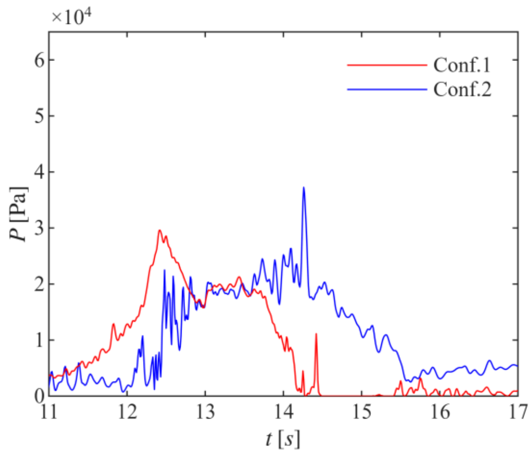

Fig. 18: pressure time histories at z_{P1} for Configurations 1 and 2.
Source: created by the authors.

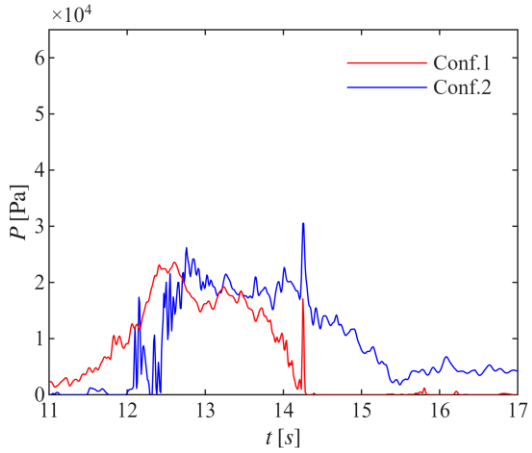

Fig. 19: pressure time histories at z_{P2} for Configurations 1 and 2.
Source: created by the authors.

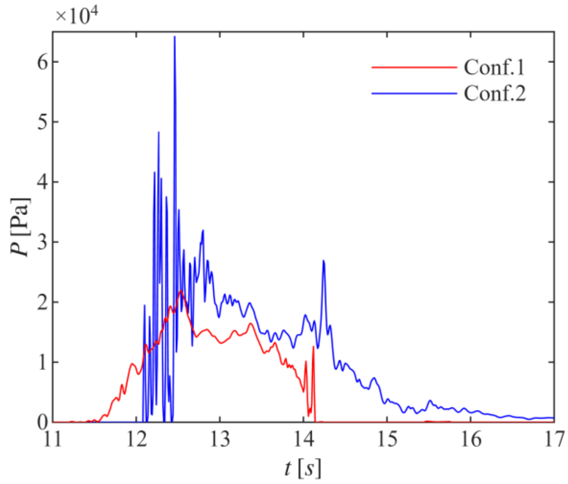

Fig. 20: pressure time histories at z_{P3} for Configurations 1 and 2.

Source: created by the authors.

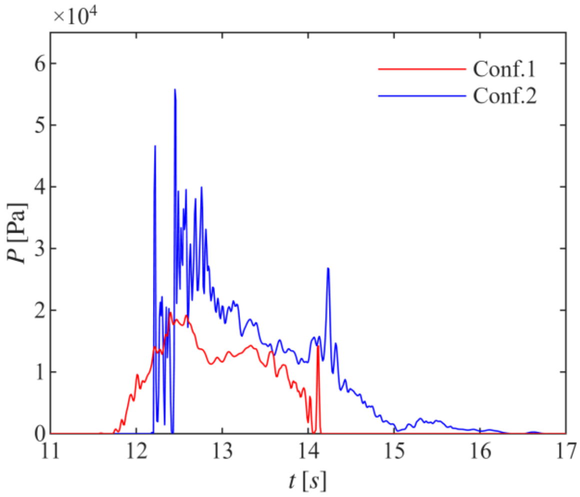

Fig. 21: pressure time histories at z_{P4} for Configurations 1 and 2.

Source: created by the authors.

Table 8. Peak pressure values obtained from the numerical simulations for Configurations 1 and 2 with $H_{w2} = 1.50\,m$.

$sensor$	$P_{max}\ [Pa]$	
	Conf.1	Conf.2
z_{P_1}	29614	37257
z_{P_2}	23597	30530
z_{P_3}	21910	64221
z_{P_4}	19644	55787

Source: created by the authors.

Table 9. Pressure impulse values obtained from the numerical simulations for Configurations 1 and 2 with $H_{w2} = 1.50\,m$.

$sensor$	$I\ [Pa \cdot s]$	
	Conf.1	Conf.2
z_{P_1}	41355	41565
z_{P_2}	37101	40250
z_{P_3}	30252	6689
z_{P_4}	26259	6880

Source: created by the authors.

Table 10. Significant pressure rise-time values obtained from the numerical simulations for Configurations 1 and 2 with $H_{w2} = 1.50\,m$.

$sensor$	$rt\ [s]$	
	Conf.1	Conf.2
z_{P_1}	0.27	1.46
z_{P_2}	0.44	1.79
z_{P_3}	0.45	0.25
z_{P_4}	0.26	0.24

Source: created by the authors.

4.3 Discussion of Results and Conclusions

This section discusses the results obtained in Sections 4.1 and 4.2, concerning the impact between solitary waves ($H_{w1} = 1.25\,m$, $H_{w2} = 1.50\,m$) and vertical walls under different seabed configurations (Conf.1, Conf.2).

Seabed Configuration 1 does not induce wave breaking for either of the two tested waves. The pressure signals (red lines) recorded at the four measurement points exhibit a regular trend, without isolated peaks or rapid decay phases, [41]. The maximum recorded values are consistent with hydrostatic pressure distributions obtained by assuming a maximum run-up equal to twice the height of the incident wave. Configuration 2 induces wave breaking for both tested waves. In this case, the pressure signals (blue lines) exhibit a markedly irregular trend. For sensors z_{P_3} and z_{P_4}, located above the still-water level, the corresponding pressure signals are characterized by the presence of sharp peaks occurring over very short rise times and decaying equally rapidly [41]. In Configuration 2, for both waves ($H_{w1} = 1.25\,m$, $H_{w2} = 1.50\,m$), the maximum pressure value is recorded by the sensor z_{P_3} located above the still-water level.

Comparing the results obtained for the two waves, similar trends can be observed in terms of the spatial distribution of the pressures and the impulses induced by wave impact. The incident wave height, H_w, is confirmed to be a key parameter governing the impact dynamics, both in the case of non-breaking waves (Conf.1) and breaking waves (Conf.2).

References:

[1] Y. Goda, Random seas and design of maritime structures, World Scientific Publishing Company, Singapore, 2010, ISBN: 981-310-102-4.

[2] M. Sainflou, Essai sur les digues maritimes verticales, Annales des Ponts et Chaussées: partie 1, mémoires et documents relatifs à l'art des constructions et au service de l'ingénieur, Vol. 98, Tome II, 1928 (4), pp. 5-48.

[3] D. D. B. Gaillard, Wave action in relation to engineering structures, Professional Paper No. 31, US Government Printing Office, Washington, DC, USA, 1904.

[4] G. Cannata, F. Palleschi, B. Iele, and F. Gallerano, A Wave-Targeted Essentially Non-Oscillatory 3D Shock-Capturing Scheme for Breaking Wave Simulation, Journal of Marine Science and Engineering, Vol.10, No.6, 2022, p. 810. https://doi.org/10.3390/jmse10060810.

[5] C. Rajasekaran, S. A. Sannasiraj, and V. Sundar, Breaking wave impact pressure on a vertical wall, The International Journal of Ocean and Climate Systems, Vol.1, No.3–4, 2010, pp. 155–166. https://doi.org/10.1260/1759-3131.1.3-4.155.

[6] H. Oumeraci, P. Klammer, and H. W. Partenscky, Classification of breaking wave loads on vertical structures, Journal of Waterway, Port, Coastal, and Ocean Engineering, Vol.119, No.4, 1993, pp. 381–397. https://doi.org/10.1061/(ASCE)0733-950X(1993)119:4(381).

[7] Y. Ito, Stability of Mixed-Type Breakwater: A Method of "Probable Sliding Distance", Coastal Engineering in Japan, Vol.14, No.1, 1971, pp. 53–61. https://doi.org/10.1080/05785634.1971.11924126.

[8] S. Takahashi, A proposal of impulsive pressure coefficient for the design of composite breakwaters, Proc. Int. Conf. Hydro-Technical Eng. Port Harbour Construction (Hydro-Port'94), Yokosuka, Japan, 1994, pp. 489-504.

[9] R. A. Bagnold, Interim Report on Wave-Pressure Research (Includes Plates and Photographs), Journal of the Institution of Civil Engineers, Vol.12, No.7, 1939, pp. 202–226. https://doi.org/10.1680/ijoti.1939.14539.

[10] K. Tanimoto, S. Takahashi, and T. Kitatani, Experimental study of impact breaking wave forces on a vertical-wall caisson of composite breakwater, Report of Port and Harbour Research Institute, Vol.20, No.2, 1981, pp. 3–39.

[11] D. H. Peregrine, Water-wave impact on walls, Annual Review of Fluid Mechanics, Vol.35, No.1, 2003, pp. 23–43. https://doi.org/10.1146/annurev.fluid.35.101101.161153.

[12] P. J. Lynett, T.-R. Wu, and P. L.-F. Liu, Modeling wave runup with depth-integrated equations, Coastal Engineering, Vol.46, No.2, 2002, pp. 89–107. https://doi.org/10.1016/S0378-3839(02)00066-9.

[13] L. H. Holthuijsen, Waves in oceanic and coastal waters, Cambridge University Press, Cambridge, UK, 2010, ISBN: 978-0521860284.

[14] Y.-T. Wu, Breaking solitary wave impact on a vertical seawall, Water, Vol.14, No.4, 2022, p. 583. https://doi.org/10.3390/w14040583.

[15] C. W. Hirt and B. D. Nichols, Volume of fluid (VOF) method for the dynamics of free boundaries, Journal of Computational Physics, Vol.39, No.1, 1981, pp. 201–225. https://doi.org/10.1016/0021-9991(81)90145-5.

[16] L. M. Gísladóttir, M. Castellino, D. Dermentzoglou, M. A. Hendriks, P. De Girolamo, M. R. Van Gent, and A. Antonini, Curved concrete crownwalls on vertical breakwaters under impulsive wave load: Finite Element Analysis, Coastal Engineering, Vol.201, 2025, Article 104791. https://doi.org/10.1016/j.coastaleng.2025.104791.

[17] S. Osher and J. A. Sethian, Fronts propagating with curvature-dependent speed: Algorithms based on Hamilton-Jacobi formulations, Journal of Computational Physics, Vol.79, No.1, 1988, pp. 12–49. https://doi.org/10.1016/0021-9991(88)90002-2.

[18] Z. Wang, J. Yang, B. Koo, and F. Stern, A coupled level set and volume-of-fluid method for sharp interface simulation of plunging breaking waves, International Journal of Multiphase Flow, Vol.35, No.3, 2009, pp. 227–246. https://doi.org/10.1016/j.ijmultiphaseflow.2008.11.005.

[19] M. Derakhti, J. T. Kirby, F. Shi, and G. Ma, NHWAVE: Consistent boundary conditions and turbulence modeling, Ocean Modelling, Vol.106, 2016, pp. 121–130. https://doi.org/10.1016/j.ocemod.2016.08.004.

[20] G. Cannata, F. Biondi, and M. Simone, Numerical Study on the Performance of an OWC under Breaking and Non-Breaking Waves, Journal of Marine Science and Engineering, Vol.12, No.6, 2024, pp. 936. https://doi.org/10.3390/jmse12060936.

[21] F. Gallerano, F. Palleschi, B. Iele, and G. Cannata, A three-dimensional high-order numerical model for the simulation of the interaction between waves and an emerged barrier, WSEAS Transactions on Fluid Mechanics, Vol.17, 2022, pp. 128–139. https://doi.org/10.37394/232013.2022.17.13.

[22] G.-R. Liu, Meshfree methods: moving beyond the finite element method, CRC Press, Boca Raton, FL, 2009, ISBN: 978-1420082098.

[23] M. Liu and G.-R. Liu, Particle methods for multi-scale and multi-physics, World Scientific, Singapore, 2015, ISBN: 978-9814578585.

[24] C. Altomare, A. J. Crespo, J. M. Domínguez, M. Gomez-Gesteira, T. Suzuki, and T. Verwaest, Applicability of Smoothed Particle Hydrodynamics for estimation of sea wave impact on coastal structures, Coastal Engineering, Vol.96, 2015, pp. 1–12. https://doi.org/10.1016/j.coastaleng.2014.12.007.

[25] L. B. Lucy, A numerical approach to the testing of fusion processes, Astronomical Journal, Vol.82, 1977, pp. 1013–1024. https://doi.org/10.1086/112164.

[26] J. J. Monaghan, Smoothed particle hydrodynamics, Annual Review of Astronomy and Astrophysics, Vol.30, 1992, pp. 543–574. https://doi.org/10.1146/annurev.aa.30.090192.002551.

[27] J. J. Monaghan, Simulating free surface flows with SPH, Journal of Computational Physics, Vol.110, No.2, 1994, pp. 399–406. https://doi.org/10.1006/jcph.1994.1034.

[28] N. J. Quinlan, M. Basa, and M. Lastiwka, Truncation error in mesh- free particle methods, International Journal for Numerical Methods in Engineering, Vol.66, No.13, 2006, pp. 2064–2085. https://doi.org/10.1002/nme.1606.

[29] D. I. Graham and J. P. Hughes, Accuracy of SPH viscous flow models, International Journal for Numerical Methods in Fluids, Vol.56, No.8, 2008, pp. 1261–1269. https://doi.org/10.1002/fld.1486.

[30] X. Zheng, W. Duan, and Q. Ma, A new scheme for identifying free surface particles in improved SPH, Science China Physics, Mechanics and Astronomy, Vol.55, No.8, 2012, pp. 1454–1463. https://doi.org/10.1007/s11433-012-4786-9.

[31] G. Oger, M. Doring, B. Alessandrini, and P. Ferrant, An improved SPH method: Towards higher order convergence, Journal of Computational Physics, Vol.225, No.2, 2007, pp. 1472–1492. https://doi.org/10.1016/j.jcp.2006.10.021.

[32] S. J. Lind, R. Xu, P. K. Stansby, and B. D. Rogers, Incompressible smoothed particle hydrodynamics for free-surface flows: A generalised diffusion-based algorithm for stability and validations for impulsive flows and propagating waves, Journal of Computational Physics, Vol.231, No.4, 2012, pp. 1499–1523. https://doi.org/10.1016/j.jcp.2011.10.012.

[33] G. Fourtakas, J. M. Dominguez, R. Vacondio, and B. D. Rogers, Local uniform stencil (LUST) boundary condition for arbitrary 3-D boundaries in parallel smoothed particle hydrodynamics (SPH) models, Computers & Fluids, Vol.190, 2019, pp. 346–361. https://doi.org/10.1016/j.compfluid.2019.06.009.

[34] H. Wendland, Piecewise polynomial, positive definite and compactly supported radial functions of minimal degree, Advances in Computational Mathematics, Vol.4, No.1, 1995, pp. 389–396. https://doi.org/10.1007/BF02123482.

[35] R. A. Dalrymple and B. D. Rogers, Numerical modeling of water waves with the SPH method, Coastal Engineering, Vol.53, No.2–3, 2006, pp. 141–147. https://doi.org/10.1016/j.coastaleng.2005.10.004.

[36] M. Antuono, A. Colagrossi, S. Marrone, and D. Molteni, Free-surface flows solved by means of SPH schemes with numerical diffusive terms, Computer Physics Communications, Vol.181, No.3, 2010, pp. 532–549. https://doi.org/10.1016/j.cpc.2009.11.002.

[37] S. Koshizuka and Y. Oka, Moving-particle semi-implicit method for fragmentation of incompressible fluid, Nuclear Science and Engineering, Vol.123, No.3, 1996, pp. 421–434. https://doi.org/10.13182/NSE96-A24205.

[38] E. Y. Lo and S. Shao, Simulation of near-shore solitary wave mechanics by an incompressible SPH method, Applied Ocean Research, Vol.24, No.5, 2002, pp. 275–286. https://doi.org/10.1016/S0141-1187(02)00054-3.

[39] L. Lobovský, E. Botia-Vera, F. Castellana, J. Mas-Soler, and A. Souto-Iglesias, Experimental investigation of dynamic pressure loads during dam break, Journal of Fluids and Structures, Vol.48, 2014, pp. 407–434. https://doi.org/10.1016/j.jfluidstructs.2014.03.005.

[40] E. Didier, D. Neves, R. Martins, and M. G. Neves, Wave interaction with a vertical wall: SPH numerical and experimental modeling, Ocean Engineering, Vol.88, 2014, pp. 330–341. https://doi.org/10.1016/j.oceaneng.2014.07.003.

[41] N. W. H. Allsop, D. Vicinanza, and J. E. McKenna, Wave Forces on Vertical and Composite Breakwaters, HR Wallingford Report SR 443, Wallingford, UK, 1996.

Contribution of Individual Authors to the Creation of a Scientific Article (Ghostwriting Policy)

- Leopoldo Ancora contributed to the implementation of the numerical methodology, contributed to writing the original draft, performed the numerical simulations, and carried out the formal analysis and visualization of the results.
- Giovanni Cannata conceptualized the study, contributed to the implementation of the numerical methodology, contributed to writing the original draft, and supervised the research activity.

Sources of Funding for Research Presented in a Scientific Article or Scientific Article Itself

No funding was received for conducting this study.

Conflict of Interest

The authors have no conflicts of interest to declare that are relevant to the content of this article.